Spin Nernst magnetoresistance for magnetization study of $FePS_3$

F. Feringa,* J. M. Vink, and B. J. van Wees†
Physics of Nanodevices, Zernike Institute for Advanced Materials, University of Groningen, 9747 AG Groningen, The Netherlands

(Received 24 December 2022; revised 21 February 2023; accepted 13 March 2023; published 24 March 2023)

The magnetization of the antiferromagnetic van der Waals material $FePS_3$ is investigated via the spin Nernst magnetoresisance (SNMR) and spin Seebeck effect (SSE). A heater and Pt detector strips are fabricated on top of a $FePS_3$ flake which generates a temperature gradient in $FePS_3$ and in the Pt detector strips. We are able to detect the SNMR in Pt, which is an interface effect, and detect the SSE response, which is a bulk effect. We conclude that there are uncompensated magnetic moments in $FePS_3$ at the interface with Pt. Via the SNMR we are able to extract the real and imaginary parts of the spin mixing conductance assuming a fully uncompensated top layer. For an in-plane thermal conductivity of 10 W/(m K) and therefore a temperature gradient of 6000 K/m in Pt we find that $G_r = 1.9 \pm 0.06 \times 10^{13}\ \Omega^{-1}\,\mathrm{m}^{-1}$ and $G_i = 4.8 \pm 0.02 \times 10^{11}\ \Omega^{-1}\,\mathrm{m}^{-1}$. In addition, the temperature gradient in $FePS_3$ generates a magnon current in $FePS_3$ via the SSE which can be detected by the Pt detector strips. We are able to extract a magnon diffusion length of 1.3 ± 0.5 and 0.5 ± 0.1 μm for thermally generated magnons in $FePS_3$ for 40 and 20 nm thicknesses, respectively.

DOI: 10.1103/PhysRevB.107.094428

I. INTRODUCTION

Spintronics aims to develop and add new functionalities to conventional electronics using the spin property of the electron [1]. Especially, magnetic two-dimensional materials are currently of great interest, for example, to develop new memory types [2]. Crucial for the development of new spintronic devices is to understand the static and dynamic properties of the magnetic materials and to characterize the interface qualities to adjacent materials, which is directly related to device performance.

Characterizing interfaces between magnetic van der Waals materials and heavy metals is also important to understand the creation and detection of spin currents in magnetic materials. The interaction between the electron spins in a heavy metal and a magnetic spin texture is governed by the spin mixing conductance $G_{\uparrow\downarrow} = G_r + iG_i$ [3], which consists of a real (G_r) and imaginary (G_i) part. G_r describes the absorption of the spin component perpendicular to $\vec{m}$ whereas G_i describes the precession of the perpendicular component of the spins around $\vec{m}$. The values of G_r and G_i can be determined using spin Hall magnetoresistance (SMR) measurements [4–6] or spin Nernst magnetoresistance measurements (SNMR) [7–9]. In both effects, the voltage across the heavy metal (HM) strips is changed due to the spin injection and detection at the interface, where both effects interact with the individual spins of the magnet. The difference between SMR and SNMR is the driving force of the spin current in the heavy metal; for SMR the spin current is generated by a charge current via the spin Hall effect whereas for the SNMR the spin current is generated via a temperature gradient in the heavy metal via the spin Nernst effect [7–10]. SMR has proven to be an excellent tool to electrically study the magnetic structures of ferromagnets [4,11], antiferromagnets [12], paramagnets [13], and especially useful to study the magnetic structures of flakes of van der Waals magnets, for example $CrPS_4$ [14] and $FePS_3$ [15].

In this paper, we show that also the spin Nerst magnetoresistance (SNMR) can be used to study the magnetization texture in a van der Waals antiferromagnet. We study the SNMR generated in a Pt detector strip on top of the antiferromagnet $FePS_3$, separated a few micrometers from a heater strip. The advantage of SNMR in a nonlocal geometry over SMR in a local geometry is that there are no spurious magnetoresistance effects in the detector strip because no current flows through the detector strip.

II. EXPERIMENTAL DETAILS

The transition metal trichalcogenide $FePS_3$ was bought from the company HQ Graphene [16]. $FePS_3$ is a uniaxial antiferromagnet with the easy axis perpendicular to the crystal layers, as shown in Fig. 1(a). The crystals were magnetically characterized using a magnetic property measurement system to extract the Néel temperature of 120 K, shown in the Appendix of Ref. [15] in which the same devices are measured. The response of the magnetic sublattices to an applied magnetic field is presented in Figs. 1(b) and 1(c). The canting angle $\theta_\perp$ is small for fields applied up to 7 T and no saturation of the in-plane magnetization is expected [18] (see below for more details). Therefore, for an in-plane applied magnetic field, a small magnetization in the x (m_x) and y (m_y) is present whereas the largest part of the magnetic moments of the individual sublattices points in the $\pm z$ (m_z) direction.

The crystals were mechanically exfoliated [19] onto a $Si\text{-}SiO_2$ substrate in a nitrogen atmosphere to prevent any

*F.Feringa@rug.nl
†B.J.van.Wees@rug.nl

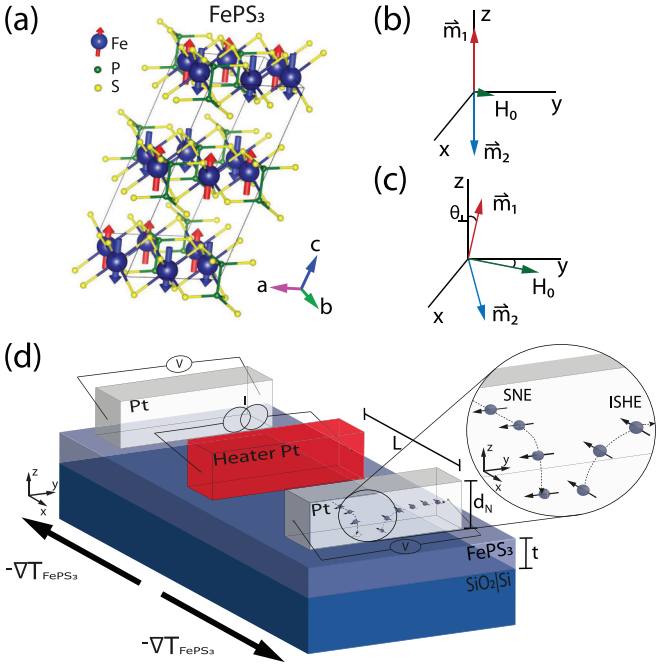

FIG. 1. (a) Crystal structure of $FePS_3$ with the spin orientation of the Fe^{2+} magnetic moments indicated by the red and blue arrows at zero magnetic field. The magnetic easy axis is perpendicular to the crystallographic **a**-**b** plane. The crystal structure is generated by VESTA [17]. (b), (c) Response of the magnetic moments of the sublattices of $FePS_3$ to an applied magnetic field. (d) Geometry of the measured devices. A charge current is send through a Pt heater to induce a temperature gradient in $FePS_3$, generating magnons via the spin Seebeck effect and a temperature gradient in the Pt detector strips generating a spin current via the spin Nernst effect. The inset shows the generated spin currents in the Pt detector strips. The second harmonic voltage responses are measured simultaneously across the two detector strips. An applied magnetic field is rotated in the *x*-*y* plane.

oxidation. The used $FePS_3$ flakes are 20 and 35 nm thick. Here, 7-nm-thick Pt strips, with widths of 200 nm, were sputtered on the flakes as the heater and detector electrodes. The center-to-center distance (L) between the Pt heater and detector electrodes varies for the different devices between 1 μm up to 5 μm. An illustration of a device is shown in Fig. 1(b), along with the electrical connections. The Pt contacts were connected to Ti (5 nm)-Au(50 nm) leads, which were evaporated on top. The Ti-Au leads are wirebonded onto a chip carrier.

An alternating current (I) was sourced through the Pt heater generating a temperature gradient in $FePS_3$ and in the Pt detector strip. The second harmonic (2ω) voltage response was measured across the Pt detector strips using lock-in amplifiers. At the Pt detector strip, a spin current is generated via the spin Nernst effect (SNE) due to the temperature gradient in the detector strip. Furthermore, the temperature gradient in $FePS_3$ generates a magnon spin current in $FePS_3$ due to the spin Seebeck effect.

The SNE generates a spin current in Pt with the spin polarization direction perpendicular to the temperature gradient: $\vec{J}_s \propto \vec{\nabla} T \times \vec{\sigma}$. Therefore in our device geometry, a spin current carried by electrons moving in the $\hat{z}$ direction is generated by a temperature gradient in the $\hat{x}$ direction with spins polarized in the $\hat{y}$ direction. A spin accumulation is generated at the Pt-$FePS_3$ interface and interacts with the magnetic moments of $FePS_3$. The spins with a polarization perpendicular to the magnetization direction are absorbed and precessed, described by G_r and G_i. The absorbed spins modulate the voltage across the Pt strip depending on the magnetization direction of $FePS_3$.

The transverse voltage response, with respect to ∇T_x, in Pt due to the SNMR is given by

$$\Delta V_{xy} = \frac{1}{2} \sum_{X=A,B} -\left(\Delta S_2 m_x^X m_y^X + \Delta S_3 m_z^X\right) \nabla T_x, \qquad (1)$$

where m_x, m_y, and m_z are the components of the magnetic moments in the x, y, and z directions of the individual sublattices A and B. The magnitude of the in-plane magnetization component is given by $\sin\theta_\perp = \frac{H_0}{2H_E + H_A}$ [20], where $\theta_\perp$ is the angle as defined in Fig. 1(c), H_0 is the applied magnetic field, and H_E and H_A are the effective exchange and anisotropy fields which are $H_E = 277$ T, and $H_A = 585$ T for $FePS_3$ [18,21]. ∇T_x is the temperature gradient in Pt in the x direction, and ΔS_2 and ΔS_3 are given by

$$\Delta S_2 = \theta_{SH}\theta_{SN} S_{HM} \frac{2\lambda}{d_N} \mathrm{Re}\left[\frac{2\lambda G_{\uparrow\downarrow} \tanh^2 \frac{d_N}{2\lambda}}{\sigma + 2\lambda G_{\uparrow\downarrow} \coth^2 \frac{d_N}{2\lambda}}\right], \qquad (2)$$

$$\Delta S_3 = -\theta_{SH}\theta_{SN} S_{HM} \frac{2\lambda}{d_N} \mathrm{Im}\left[\frac{2\lambda G_{\uparrow\downarrow} \tanh^2 \frac{d_N}{2\lambda}}{\sigma + 2\lambda G_{\uparrow\downarrow} \coth^2 \frac{d_N}{2\lambda}}\right], \qquad (3)$$

where λ, d_N, and σ are the spin relaxation length in the HM, thickness of the HM, and the bulk conductivity of the HM, respectively. θ_{SH}, θ_{SN}, and S_{HM} are the spin Hall angle, spin Nernst angle, and the Seebeck coefficient of the HM. An important difference between the SNMR and the SMR is that the SMR is independent of the sign of the spin Hall angle because the generation and detection of the spin current is via the (inverse) spin Hall effect [(I)SHE] whereas the SNMR depends on the product of the spin Nernst angle and the spin Hall angle because the spin current is generated via the SNE and detected via the ISHE.

A temperature gradient in the van der Waals magnets generates an imbalance in the magnon population which results in a magnon spin current. This effect is called the spin Seebeck effect (SSE) [22–25]. It is assumed that the magnons are predominately generated close to the heater and are transported over a certain distance to the detector. The magnon current is detected via spin-flip scattering of the magnons with the electrons in a heavy metal generating a spin accumulation at the interface [26]. This spin accumulation is then turned into a charge current via the inverse spin Hall effect generating a voltage difference over the detector strip [27].

The thermally generated magnons in $FePS_3$, via the SSE, arrive at the detector strip and interact with the electrons in the detector strip generating a spin accumulation. The spin accumulation in the detector strip is converted into a charge current via the ISHE. The spins carried by the magnons are polarized in the direction of the magnetization of $FePS_3$ induced by the applied magnetic field. Next to that, the magnitude of the SSE is expected to be proportional to the magnitude of

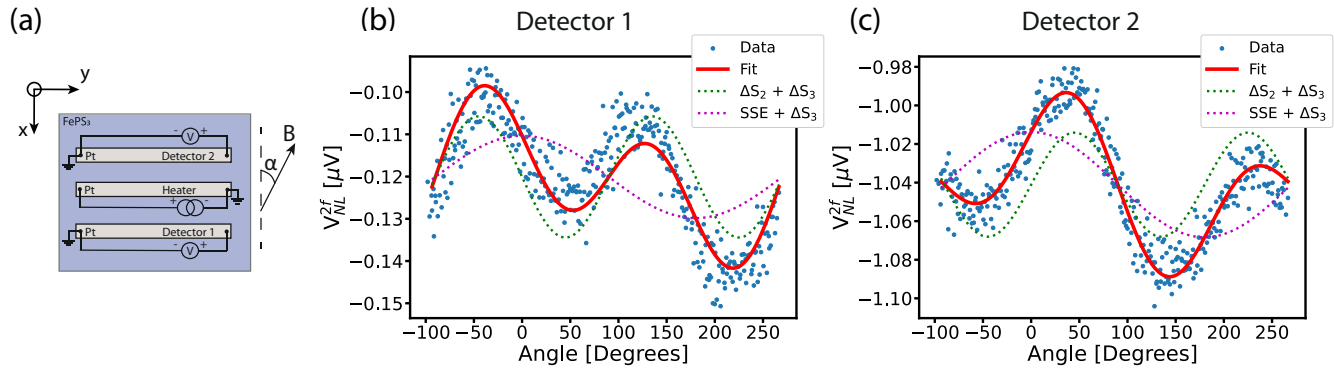

FIG. 2. (a) Device overview with the connections of the current and voltage probes and the orientation of the magnetic field with respect to the heater and detector strips. The current density in the heater strip is 7×10^8 A/m^2. (b) and (c) Second harmonic response across detector strips 1 and 2 for a rotation of the applied magnetic field in plane. The solid line represents the fit of the data with Eq. (4) and the dashed lines show the different components within the fit, representing the SNMR and SSE contribution. The direction of ∇T_x is opposite for detectors 1 and 2, therefore the sign of the SNMR contribution is opposite whereas the sign of the SSE is equal for detectors 1 and 2.

the in-plane magnetization. The voltage response due to the ISHE is maximum when the spin polarization of the spin accumulation is perpendicular to the detector strip. Therefore the detected voltage due to the SSE depends on the orientation of the magnetization with respect to the detector strip and is maximum when the magnetic field is perpendicular to the detector strip.

III. RESULTS AND DISCUSSION

The second harmonic responses are measured across a detector strip for an in-plane rotating external applied magnetic field as shown in Fig. 2. The response consists of a contribution of the SNMR in Pt and a contribution of the SSE. Both contributions depend on the orientation of the magnetization with respect to the detector strip, which is expressed as

$$V_{2\omega}(\alpha) = \Delta S_2 \cos(\alpha)\sin(\alpha) + \Delta V_{\mathrm{SSE}} \cos(\alpha) + \Delta S_3, \quad (4)$$

where ΔS_2 and ΔS_3 represent the contribution of the SNMR as expressed in Eq. (1) and ΔV_{SSE} is the amplitude of the SSE contribution. ΔS_3 does not depend on the in-plane orientation (angle α) of the applied magnetic field only on the magnitude of the applied field and therefore represents the offset voltage of the second harmonic response. An interesting result is that we expect the contribution of ΔS_3 to be zero, because m_z is opposite for each sublattice and therefore the net contribution would be zero. However, ΔS_3 shows a clear contribution to the detected voltage below the Néel temperature and disappears above the Néel temperature. Both contributions, $\Delta S_2 + \Delta S_3$ and $\Delta V_{\mathrm{SSE}} + \Delta S_3$, are plotted as dashed lines in Fig. 2 and the fit of Eq. (4) is the solid red line in Fig. 2. Note that the sign of the ΔS_2 depends on the direction of the temperature gradient with respect to the detector strip whereas the sign due to the SSE is independent of the direction of the temperature gradient. This allows for a clear distinction between the SNMR and the SSE. The subsequent results presented are the absolute values of ΔS_2, i.e., corrected for the sign of the temperature gradient. Any anisotropic magnetoresistance effects in Pt have been excluded in previous measurements on the same devices [15].

The SNMR and SSE contributions have been measured for various temperatures and applied magnetic field strengths, as shown in Fig. 3. The SNMR contribution shows a clear increase with magnetic field strength indicating the canting of the magnetic moments in the direction of the magnetic field, and therefore increasing the magnitude of $m_x m_y$. The magnitude of the SSE response is expected to be proportional to the magnitude of the net magnetization, which we note is not consistent with the measured response. It shows an increase at low fields, but starts to saturate or decrease around 3 T where we expect a continuous increase, similar to the SNMR signal.

The temperature-dependent measurements show a clear decrease with increasing temperature. ΔS_2, ΔS_3, and ΔV_{SSE} go to zero when reaching the Néel temperature of $FePS_3$ at 120 K, clearly indicating that all three effects are related to the magnetic ordering of $FePS_3$. The ΔV_{SSE} decreases with increasing temperatures, which is attributed to a decrease of the thermal conductivity of $FePS_3$ for increasing temperatures [28]. Note that Wimmer *et al.* [10] report a vanishing spin Nernst effect at lower temperatures which is different from our results.

The second harmonic response has been measured for various heater-detector distances where the ΔV_{SSE} with respect to heater-detector distance is plotted in Fig. 4. We expect the decay for the magnon signal, when the magnon currents are generated in proximity of the heater strip via the SSE and are transported to the detector strip, to be [26,29]

$$V_{\mathrm{SSE}} = C \exp -L/\lambda_{\mathrm{m}}, \quad (5)$$

where λ_{m} is the magnon diffusion length, L is the heater-detector distance, and C contains the distance-independent parameters. The solid lines in Fig. 4 represent the fits for the data from flakes 2 and 3 which give magnon diffusion lengths for the thermally excited magnons of 0.5 ± 0.1 and 1.3 ± 0.5 μm, respectively. The diffusion length decreases with decreasing thickness, similar to what is observed for flakes of $MnPS_3$ [29], but opposite to what is observed for yttrium iron garnet (YIG) [24]. The diffusion length is between 5 and 15 times smaller than for the thermally generated magnons in

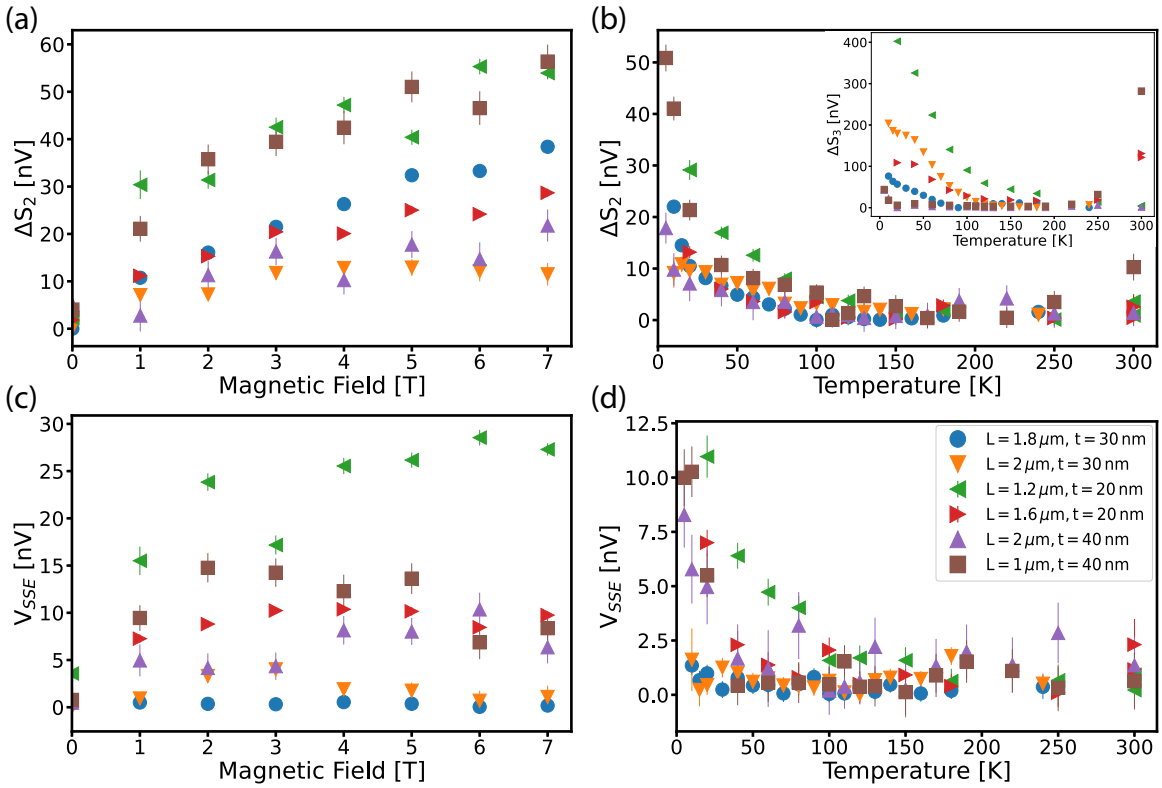

FIG. 3. (a) and (c) Magnetic-field-dependent response of ΔV_{SSE} and ΔS_2 for various distances between the heater and detector (L) and two flake thicknesses of $FePS_3$ (t) at 5 K. (b) and (d) Temperature-dependent response of ΔV_{SSE} and ΔS_2 for various distances between the heater and detector (L) and two flake thicknesses of $FePS_3$ (t) at 7 T. The inset in (b) shows the temperature dependence of ΔS_3, which disappears above the Néel temperature.

200-nm-thick YIG film and comparable to thin flakes (8 nm) of $MnPS_3$ [24,29].

The real and imaginary parts of the spin mixing conductance are extracted from the data by fitting Eq. (4). We expect

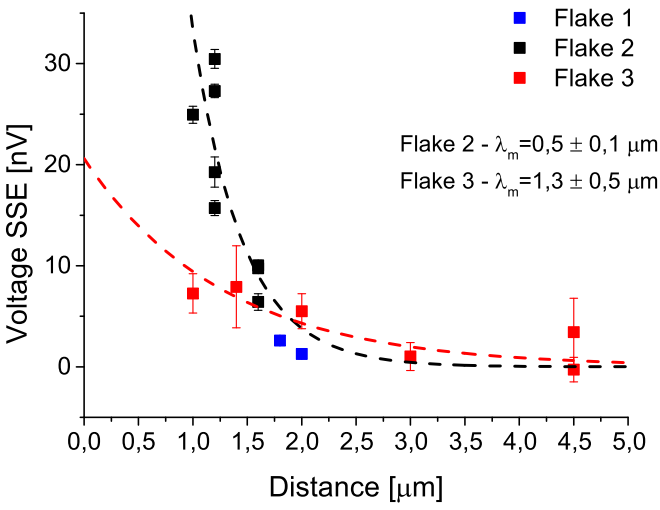

FIG. 4. Signal due to SSE vs distance between the heater and injector for different devices. Equation (5) has been fitted to the data and the magnon diffusion length λ_{m} has been extracted for both devices. Flake 1 is 30 nm thick, flake 2 is 20 nm thick, and flake 3 is 40 nm thick.

that ΔS_3 is zero for a fully compensated antiferromagnet, such as $FePS_3$, in contact with Pt. We cannot determine G_r and G_i separately from ΔS_2, noting that generally it is assumed that G_i is much smaller than G_r. However, we can determine G_r and G_i for certain ratios with respect to each other, as shown in Fig. 5. The magnitude of the temperature gradient in Pt has been obtained via a COMSOL model [30]. The thermal conductivity of $FePS_3$ at 5 K is not known. Haglund reports a thermal conductivity of 100 W/(m K) around 20 K which decreases with decreasing temperature [28]. Therefore the temperature gradient in Pt has been calculated for thermal conductivities of 1, 10, and 100 W/(m K) for $FePS_3$ and a heater power of 30 μW in the heater.

However, we measured a pronounced contribution from ΔS_3 in our measurements. This may indicate that the top layer of the $FePS_3$ flake in contact with Pt possesses uncompensated magnetic moments. We cannot determine how large the exact contribution of the uncompensated moments and therefore the magnitude of m_z is. We can look at an upper limit by treating the top layers as if it would be ferromagnetic, i.e., the m_z contribution of both sublattices points in the same direction. Now we can determine G_r and G_i separately using Eqs. (2)–(4) which are plotted in Fig. 6 for various temperature gradients. The temperature gradients correspond to the various thermal conductivities of $FePS_3$ which are indicated by the vertical lines. The inset shows the ratio between G_i and G_r.

The ratio between G_i and G_r saturates for higher temperature gradients around 0.026 ± 0.001, which is in the same

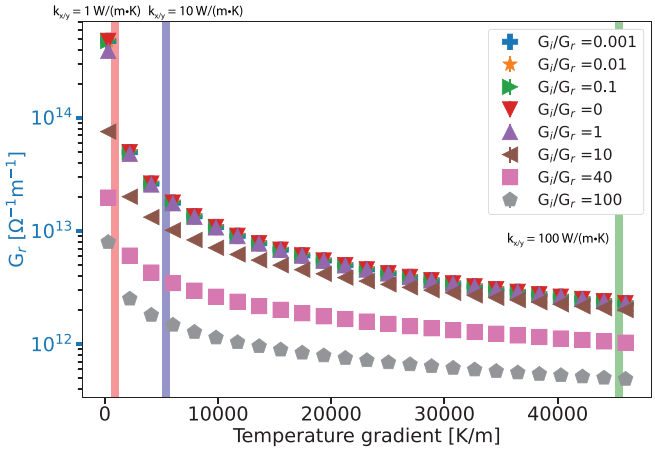

FIG. 5. The real part (G_r) of the spin mixing conductance extracted for various values of the temperature gradient in the Pt strip and for various ratios of G_i and G_r. The measured data have been fitted with Eqs. (4) and (2) using $\lambda = 1$ nm, $d_N = 7$ nm, $1/\sigma_{Pt} = 37\ \mu\Omega\,\mathrm{cm}$, $\theta_{SH} = 0.10$, $\theta_{SN} = -0.2$, $S_{HM} = -10\ \mu\mathrm{V/K}$ for Pt [7]. The red, blue, and green transparent lines indicate the temperature gradient in Pt for the thermal conductivity of $FePS_3$ of 1, 10, and 100 W/(m K), respectively.

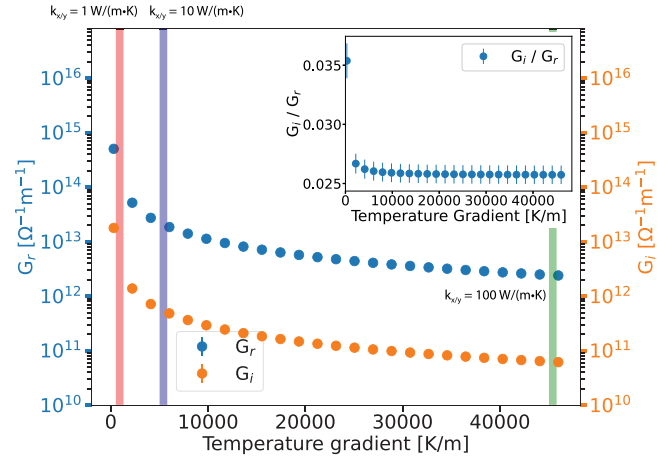

FIG. 6. The real (G_r) and imaginary (G_i) parts of the spin mixing conductance extracted for various values of the temperature gradient in the Pt strip assuming a fully uncompensated top layer of $FePS_3$. The inset shows the ratio between G_r and G_i. The measured data have been fitted with Eqs. (4), (2), and (3) using the same parameters as presented in the inset of Fig. 5.

order of magnitude as compared to a ratio of 0.06 ± 0.015 for 200-nm-thick YIG film in contact with Pt [4].

IV. CONCLUSION

In summary, using a nonlocal device geometry we detect the SNMR and SSE in Pt and $FePS_3$ simultaneously using a thermal gradient in Pt and $FePS_3$ generated by a heater strip. We are able to extract a magnon diffusion length of 1.3 ± 0.5 and 0.5 ± 0.1 μm for thermally generated magnons in $FePS_3$ for 40 and 20 nm thicknesses, respectively, which shows a decrease with decreasing thickness. We conclude that there are uncompensated magnetic moments in $FePS_3$ at the interface with Pt. Via the SNMR we are able to extract the real and imaginary part of the spin mixing conductance assuming a fully uncompensated top layer. For an in-plane thermal conductivity of 10 W/(m K) and therefore a temperature gradient of 6000 K/m in Pt we find that $G_r = 1.9 \pm 0.06 \times 10^{13}\ \Omega^{-1}\,\mathrm{m}^{-1}$ and $G_i = 4.8 \pm 0.02 \times 10^{11}\ \Omega^{-1}\,\mathrm{m}^{-1}$.

ACKNOWLEDGMENTS

We acknowledge the technical support from J. G. Holstein, H. Adema, T. Schouten, F. van der Velde, and H. de Vries. We acknowledge the financial support of the Zernike Institute for Advanced Materials and the European Union's Horizon 2020 research and innovation program under Grants Agreement No. 785219 and No. 881603 (Graphene Flagship Core 2 and Core 3). This project is also financed by the NWO Spinoza prize awarded to B.J.v.W. by the NWO and has received funding from the European Research Council (ERC) under the European Union's 2DMAGSPIN (Grant Agreement No. 101053054).

[1] A. Barman, G. Gubbiotti, S. Ladak, A. O. Adeyeye, M. Krawczyk, J. Gräfe, C. Adelmann, S. Cotofana, A. Naeemi, V. I. Vasyuchka, B. Hillebrands, S. A. Nikitov, H. Yu, D. Grundler, A. V. Sadovnikov, A. A. Grachev, S. E. Sheshukova, J.-Y. Duquesne, M. Marangolo, G. Csaba *et al.*, J. Phys.: Condens. Matter **33**, 413001 (2021).

[2] H. Yang, S. O. Valenzuela, M. Chshiev, S. Couet, B. Dieny, B. Dlubak, A. Fert, K. Garello, M. Jamet, D.-E. Jeong, K. Lee, T. Lee, M.-B. Martin, G. S. Kar, P. Sénéor, H.-J. Shin, and S. Roche, Nature (London) **606**, 663 (2022).

[3] Y. Tserkovnyak, A. Brataas, and G. E. W. Bauer, Phys. Rev. Lett. **88**, 117601 (2002).

[4] N. Vlietstra, J. Shan, V. Castel, J. Ben Youssef, G. E. W. Bauer, and B. J. van Wees, Appl. Phys. Lett. **103**, 032401 (2013).

[5] M. Althammer, S. Meyer, H. Nakayama, M. Schreier, S. Altmannshofer, M. Weiler, H. Huebl, S. Geprägs, M. Opel, R. Gross, D. Meier, C. Klewe, T. Kuschel, J.-M. Schmalhorst, G. Reiss, L. Shen, A. Gupta, Y.-T. Chen, G. E. W. Bauer, E. Saitoh *et al.*, Phys. Rev. B **87**, 224401 (2013).

[6] Y.-T. Chen, S. Takahashi, H. Nakayama, M. Althammer, S. T. B. Goennenwein, E. Saitoh, and G. E. W. Bauer, Phys. Rev. B **87**, 144411 (2013).

[7] D. J. Kim, C. Y. Jeon, J. G. Choi, J. W. Lee, S. Surabhi, J. R. Jeong, K. J. Lee, and B. G. Park, Nat. Commun. **8**, 1400 (2017).

[8] S. Meyer, Y.-T. Chen, S. Wimmer, M. Althammer, T. Wimmer, R. Schlitz, S. Geprägs, H. Huebl, D. Ködderitzsch, H. Ebert, G. E. W. Bauer, R. Gross, and S. T. B. Goennenwein, Nat. Mater. **16**, 977 (2017).

[9] A. Bose, S. Bhuktare, H. Singh, S. Dutta, V. G. Achanta, and A. A. Tulapurkar, Appl. Phys. Lett. **112**, 162401 (2018).

[10] T. Wimmer, J. Gückelhorn, S. Wimmer, S. Mankovsky, H. Ebert, M. Opel, S. Geprägs, R. Gross, H. Huebl, and M. Althammer, Phys. Rev. B **104**, L140404 (2021).
[11] N. Vlietstra, J. Shan, V. Castel, B. J. van Wees, and J. Ben Youssef, Phys. Rev. B **87**, 184421 (2013).
[12] G. R. Hoogeboom, A. Aqeel, T. Kuschel, T. T. Palstra, and B. J. Van Wees, Appl. Phys. Lett. **111**, 052409(2017).
[13] K. Oyanagi, J. M. Gomez-Perez, X. P. Zhang, T. Kikkawa, Y. Chen, E. Sagasta, A. Chuvilin, L. E. Hueso, V. N. Golovach, F. S. Bergeret, F. Casanova, and E. Saitoh, Phys. Rev. B **104**, 134428 (2021).
[14] R. Wu, A. Ross, S. Ding, Y. Peng, F. He, Y. Ren, R. Lebrun, Y. Wu, Z. Wang, J. Yang, A. Brataas, and M. Kläui, Phys. Rev. Appl. **17**, 064038 (2022).
[15] F. Feringa, G. E. W. Bauer, and B. J. van Wees, Phys. Rev. B **105**, 214408 (2022).
[16] HQ Graphene, http://www.hqgraphene.com/
[17] K. Momma and F. Izumi, J. Appl. Crystallogr. **44**, 1272 (2011).
[18] A. R. Wildes, D. Lançon, M. K. Chan, F. Weickert, N. Harrison, V. Simonet, M. E. Zhitomirsky, M. V. Gvozdikova, T. Ziman, and H. M. Rønnow, Phys. Rev. B **101**, 024415 (2020).
[19] K. S. Novoselov, D. Jiang, F. Schedin, T. J. Booth, V. V. Khotkevich, S. V. Morozov, and A. K. Geim, Proc. Natl. Acad. Sci. USA **102**, 10451 (2005).
[20] A. Gurevich and G. Melkov, *Magnetization Oscillations and Waves* (CRC Press, Boca Raton, FL, 2020).
[21] D. Lançon, H. C. Walker, E. Ressouche, B. Ouladdiaf, K. C. Rule, G. J. McIntyre, T. J. Hicks, H. M. Rønnow, and A. R. Wildes, Phys. Rev. B **94**, 214407 (2016).
[22] K. Uchida, S. Takahashi, K. Harii, J. Ieda, W. Koshibae, K. Ando, S. Maekawa, and E. Saitoh, Nature (London) **455**, 778 (2008).
[23] J. Shan, L. J. Cornelissen, J. Liu, J. B. Youssef, L. Liang, and B. J. van Wees, Phys. Rev. B **96**, 184427 (2017).
[24] J. Shan, L. J. Cornelissen, N. Vlietstra, J. Ben Youssef, T. Kuschel, R. A. Duine, and B. J. van Wees, Phys. Rev. B **94**, 174437 (2016).
[25] F. Feringa, J. M. Vink, and B. J. van Wees, Phys. Rev. B **106**, 224409 (2022).
[26] L. J. Cornelissen, J. Liu, R. A. Duine, J. B. Youssef, and B. J. van Wees, Nat. Phys. **11**, 1022 (2015).
[27] E. Saitoh, M. Ueda, H. Miyajima, and G. Tatara, Appl. Phys. Lett. **88**, 182509 (2006).
[28] A. Haglund, Ph.D. thesis, University of Tennessee, 2019.
[29] W. Xing, L. Qiu, X. Wang, Y. Yao, Y. Ma, R. Cai, S. Jia, X. C. Xie, and W. Han, Phys. Rev. X **9**, 011026 (2019).
[30] See Supplemental Material at http://link.aps.org/supplemental/10.1103/PhysRevB.107.094428 for more information about the COMSOL model.